🔓 OPEN ACCESS

Thermally stable high-loading single Cu sites on ZSM-5 for selective catalytic oxidation of NH₃

Lu Chen[a,1,2] 🆔, Xuze Guan[a,1] 🆔, Xinbang Wu[b] 🆔, Hiroyuki Asakura[c] 🆔, David G. Hopkinson[d], Christopher Allen[d,e] 🆔, June Callison[f], Paul J. Dyson[b,2] 🆔, and Feng Ryan Wang[a,2]

Affiliations are included on p. 7.

Rigorous comparisons between single site- and nanoparticle (NP)-dispersed catalysts featuring the same composition, in terms of activity, selectivity, and reaction mechanism, are limited. This limitation is partly due to the tendency of single metal atoms to sinter into aggregated NPs at high loadings and elevated temperatures, driven by a decrease in metal surface free energy. Here, we have developed a unique two-step method for the synthesis of single Cu sites on ZSM-5 (termed Cu$_S$/ZSM-5) with high thermal stability. The atomic-level dispersion of single Cu sites was confirmed through scanning transmission electron microscopy, X-ray absorption fine structure (XAFS), and electron paramagnetic resonance spectroscopy. The Cu$_S$/ZSM-5 catalyst was compared to a CuO NP-based catalyst (termed Cu$_N$/ZSM-5) in the oxidation of NH₃ to N₂, with the former exhibiting superior activity and selectivity. Furthermore, operando XAFS and diffuse reflectance infrared Fourier transform spectroscopy studies were conducted to simultaneously assess the fate of the Cu and the surface adsorbates, providing a comprehensive understanding of the mechanism of the two catalysts. The study shows that the facile redox behavior exhibited by single Cu sites correlates with the enhanced activity observed for the Cu$_S$/ZSM-5 catalyst.

heterogeneous catalysis | selective catalytic oxidation | ammonia oxidation | single site catalyst | operando spectroscopy

Compared with bulk metal catalysts, smaller-sized metal arrays, i.e., nanoparticles (NPs), clusters, and single metal sites, enhance metal usage efficiency and impact strongly on the activity and selectivity of reactions. In recent years, atomically dispersed catalysts have gained significant attention as they maximize atom utilization and have distinct and tunable structural features (1–3). Atomically dispersed metals in single-site catalysts (SSCs) composed of Earth-abundant metals tend to aggregate into larger NPs at elevated temperatures due to their excess surface free energy, a phenomenon known as thermal deactivation or sintering (4). One strategy to prevent collision and coalescence involves confining metal sites within microporous solids such as zeolites and metal-organic frameworks (5–7), a strategy which is effective at relatively low metal loadings. Moreover, SSCs demonstrate unique catalytic properties distinct from NP-based catalysts, for example, in oxidation reactions, particle size strongly influences activity and selectivity patterns (8–10). Despite the significant catalytic advancements achieved through metal isolation, few studies rigorously compare the performance of high-loading single sites (SSs)—in terms of activity and selectivity—with NP-based counterparts featuring the same composition under identical conditions. While the effects of metal particle size have been outlined, operando studies that illuminate the active sites would provide a deeper understanding of the reaction mechanisms involved (8).

Selective catalytic oxidation of NH₃ to N₂ (NH₃–SCO) is extensively used to eliminate NH₃ from oxygen-containing stationary and mobile exhausts, as the process operates under mild conditions and is highly efficient (11, 12). Suitable catalysts for the NH₃–SCO reaction should be cost-effective and highly stable for industrial applications, while enabling complete conversion of NH₃ to N₂ at low temperatures (T < 400 °C), without generating harmful NO$_x$ by-products. Among these existing catalysts, copper-based catalysts have gained considerable attention due to the abundance of copper and its outstanding performance in the SCO of NH₃ (13–16). Many studies have been devoted toward controlling active sites through the manipulation of crystal size, as a means to maximize the catalytic oxidation performance (13, 15).

Finely dispersed copper oxide species were found to be among the most efficient oxide catalysts for NH₃–SCO, but further increasing the copper loading did not improve the catalytic activity, possibly due to the formation of CuO aggregates (17, 18). Zeolites have high stabilities, high surface areas, and based on their porous nature, offer the possibility to build multifunctional catalysts. Moreover, zeolites are well-defined crystalline, tunable

Significance

Single-site-based catalysts exhibit high atom efficiency and tunable structure–activity properties. However, their real-world application remains tenuous as their activity is related to the low metal loading; otherwise, stability issues become relevant. We developed a scalable method for synthesizing thermally stable, high-loading single Cu site catalysts, which exhibit superior activity and selectivity in NH₃ oxidation compared to nanoparticle-based catalysts. A unique reaction pathway was unambiguously demonstrated for the single Cu site catalyst through operando X-ray absorption fine structure and diffuse reflectance infrared Fourier transform spectroscopy, addressing the shortcomings in fundamental mechanistic steps, which have lagged behind empirical catalysts screening. This work marks an advancement in single-site catalysis and contributes to mechanistic understanding, fostering improvements in catalyst design.

[1]L.C. and X.G. contributed equally to this work.

[2]To whom correspondence may be addressed. Email: lc962@cam.ac.uk, paul.dyson@epfl.ch, or ryan.wang@ucl.ac.uk.

supports that can play analogous roles to ligands in homogeneous catalysts and enzymatic systems, while helping to stabilize isolated metal atoms and clusters. Wang et al. showed that CuO NPs immobilized on zeolites are active in the NH₃–SCO reaction, with the activity following the order: Cu/ZSM-5 > Cu/Beta > Cu/MCM-49 > Cu/Y > Cu/MOR (mordenite) > Cu/FER (ferrierite) (13). Cu/ZSM-5 is also the most active catalyst in the NH₃-selective catalytic reduction (SCR) reaction (19–22). Therefore, in NH₃–SCO, Cu-modified zeolites follow the internal SCR (i-SCR) mechanism (23), in which ammonia is first converted to NO_x, which is then catalytically reduced to N_2 by NH_x species.

To achieve structural control and overcome drawbacks associated with the impregnation method, we report a two-step strategy to immobilize thermally stable single Cu sites (SSs) on ZSM-5 (Cus/ZSM-5) with high a Cu loading of 4 wt%. We compared the performance of the Cu SS-based Cus/ZSM-5 catalyst with a CuO NP-based catalyst (Cu_N/ZSM-5) with the same Cu loading, in the NH₃–SCO reaction. The redox behavior of the Cu SSs and CuO NPs was investigated in the NH₃–SCO reaction using operando X-ray absorption fine structure (XAFS), to disclose different reaction mechanisms and identify the catalytically active species. The different Cu intermediates in Cus/ZSM-5 and Cu_N/ZSM-5 were validated by extended XAFS (EXAFS) wavelet transform (WT) analysis and diffuse reflectance infrared Fourier transform spectroscopy (DRIFTS).

## Results and Discussion

The Cu_S/ZSM-5 catalyst was synthesized using a two-step method, which is scalable and achieves Cu contents as high as 4 wt%. The Cu precursor [$Cu(NO_3)_2 \cdot 3H_2O$] is first reduced by H_2 to form Cu clusters inside ZSM-5 and then it is annealed in air at 500 °C for 5 h leading to dispersion of the Cu and the formation of highly thermal stable Cu SSs. As a comparison, for Cu_N/ZSM-5, the Cu precursor is reduced by $NaBH_4$ to form large Cu NPs which are annealed to the surface of ZSM-5 in air at 500 °C for 5 h to form CuO NPs on the surface of ZSM-5. Cu_M/ZSM-5, which comprises a mixture of CuO NPs and Cu SSs, was synthesized by grinding the Cu precursor with ZSM-5 followed by annealing in air at 500 °C for 5 h. Since all three catalysts were annealed in air at 500 °C for 5 h, they are expected to be thermally stable.

Structural Characterization of the Catalysts. Bright field-scanning transmission electron microscopy (BF-STEM) was used to characterize the catalysts, but due to the similar Z-contrast of Cu, Si, and Al, Cu SSs are not distinguishable (Fig. 1A). Elemental mapping (EDX) images show that the Cu SSs are homogeneously distributed on the ZSM-5 support in Cus/ZSM-5 (*SI Appendix*, Fig. S1A). EDX mapping images also show the Cu remains atomically dispersed after catalysis (*SI Appendix*, Fig. S1B), see below for the catalytic studies. In comparison, in Cu_N/ZSM-5 (Fig. 1B and *SI Appendix*, Fig. S2), the CuO NPs are located on the surface of ZSM-5 with an average size of 9.7 nm, and their composition was confirmed by EDX mapping (*SI Appendix*, Fig. S3). To further confirm that the Cu atoms are atomically dispersed on ZSM-5 in Cus/ZSM-5, EXAFS and X-ray absorption near-edge structure (XANES) measurements were performed (Fig. 1 C and D). The Cu K-edge EXAFS in R space of Cu_N/ZSM-5 contains a peak at ca. 2.5 Å, which may be attributed to Cu–Cu scattering, whereas Cus/ZSM-5 has only one dominant peak at ca. 1.5 Å, corresponding to Cu–O bonds (Fig. 1D), verifying the presence of atomically dispersed Cu sites. The Cu(II) SSs content was quantified using electron paramagnetic resonance (EPR) spectroscopy employing dilute $CuSO_4 \cdot 5H_2O$ in Na_2SO_4 as an external standard. At the same Cu loading, nearly 80% of the Cu sites are in the form of Cu(II) SSs in Cus/ZSM-5, compared to 28% in Cu_M/ZSM-5 and only 8% in Cu_N/ZSM-5 (Fig. 1 E and F). Apart from 80% of Cu(II) SSs in Cus/ZSM-5, the remaining 20% of Cu species comprise CuO clusters. The Cu(II) SSs were re-examined after catalysis, and nearly identical contents of Cu(II) SSs were observed (Fig. 1 E and F), verifying the stability of Cu species in the three catalysts. However, after the reaction, the peak shifts to a higher field, implying that the chemical environment of Cu(II) SSs has changed, due to a change from H^+ balanced to NH_4^+ balanced ZSM-5. A peak at 38.9° corresponding to CuO (111) (PDF #48-1548) in the X-ray diffraction (XRD) pattern is observed in Cu_N/ZSM-5 and Cu_M/ZSM-5, confirming the presence of CuO NPs (*SI Appendix,* Fig. S4). XPS shows that the oxidation state of Cu species in Cus/ZSM-5 is different from that in Cu_N/ZSM-5 and Cu_M/ZSM-5. While the majority of Cu species in Cus/ZSM-5 are in the Cu(II) oxidation state, Cu(I) is also present, whereas only Cu(II) is present in Cu_N/ZSM-5
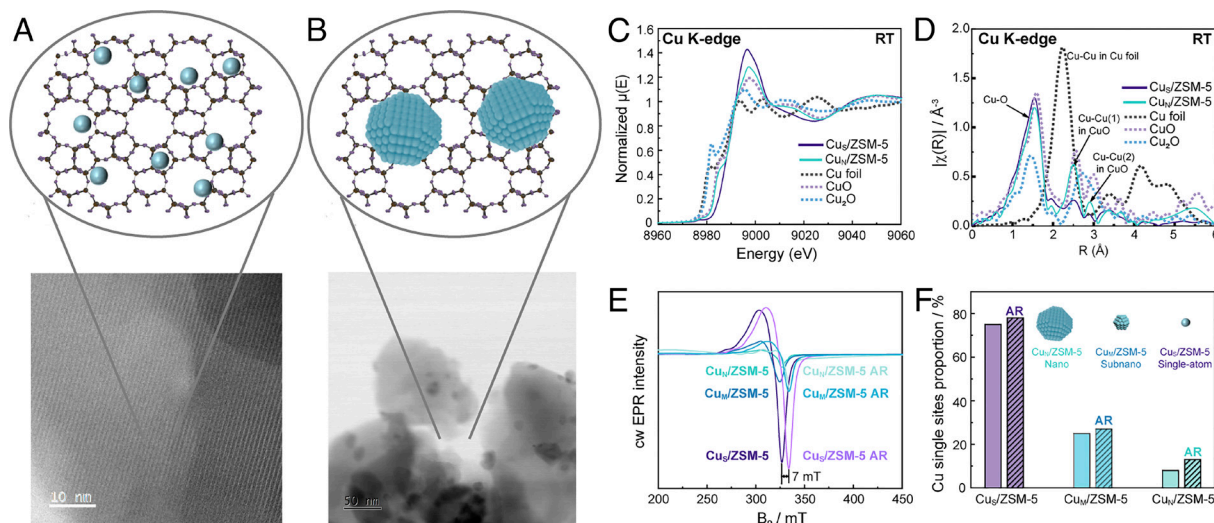
Fig. 1. Characterization of Cus/ZSM-5 and Cu_N/ZSM-5. (A and B) BF-STEM images of Cus/ZSM-5 and Cu_N/ZSM-5; (C and D) EXAFS spectra and R space spectra of the Cu K-edge EXAFS of Cus/ZSM-5 and Cu_N/ZSM-5; (E) X-band cw EPR spectra of Cus/ZSM-5, Cus/ZSM-5, and Cu_N/ZSM-5 before and after reaction (after catalytic tests, see *Materials and Methods* for further details); (F) Quantification of atomic Cu(II) sites.
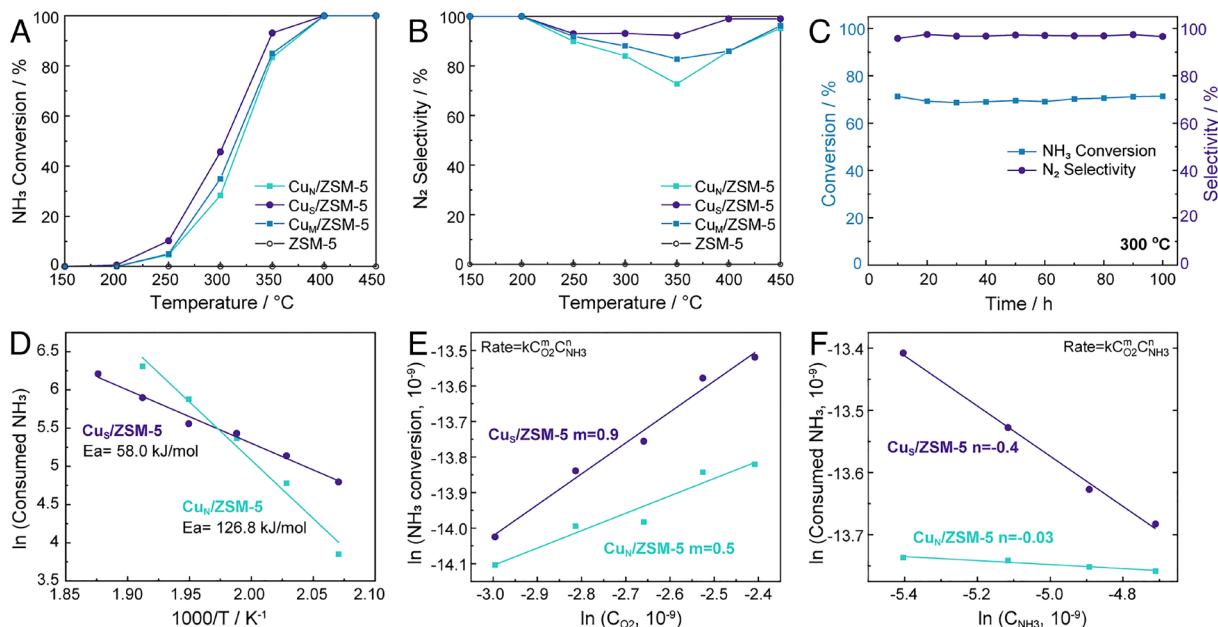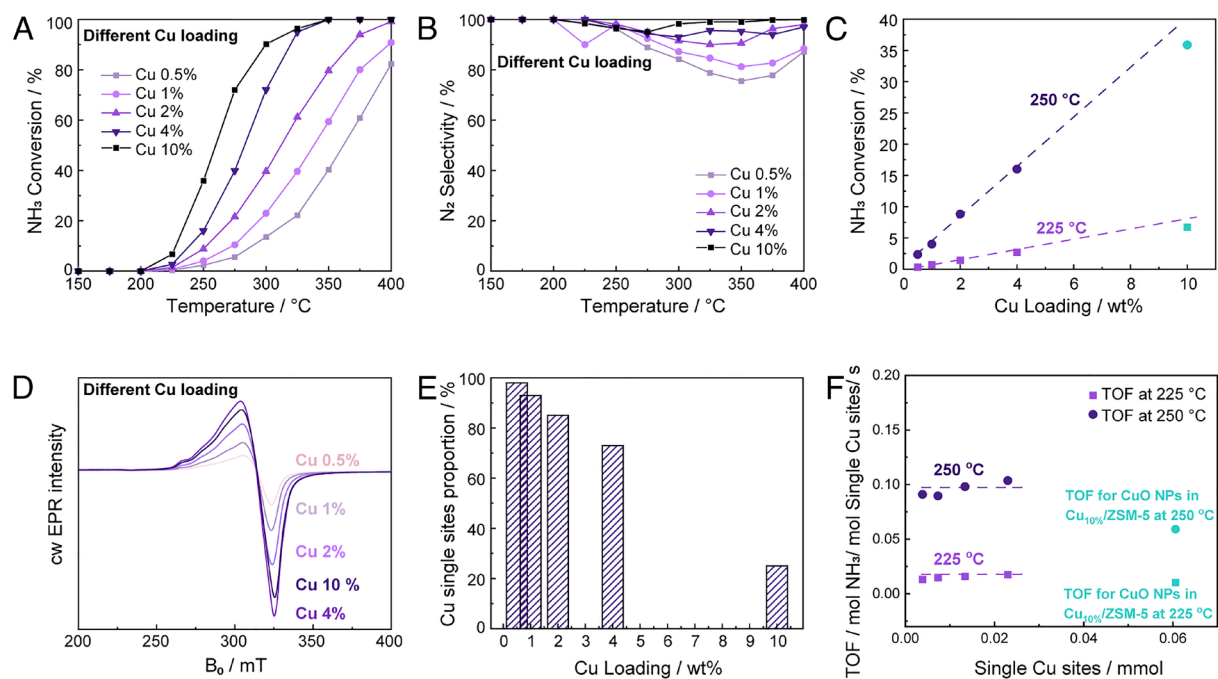
Fig. 2. Evaluation of Cu_S/ZSM-5, Cu_M/ZSM-5 and Cu_N/ZSM-5 (all 4 wt%) catalysts and ZSM-5 in NH_3–SCO. (*A* and *B*) NH_3 conversion and N_2 selectivity as a function of temperature [reaction conditions: 50 mg catalyst, 5,000 ppm NH_3, 5% O_2 balanced in He, gas flow 100 mL/min, weight hourly space velocity (WHSV) 600 mL NH_3 h^{-1} g^{-1}]; (*C*) stability tests at 300 °C for 100 h (50 mg catalyst, 2,000 ppm NH_3, 5% O_2 balanced in He, gas flow 100 mL/min); (*D*) E_a of Cu_S/ZSM-5 and Cu_N/ZSM-5; (*E*) Reaction order of O_2 for the Cu_S/ZSM-5 and Cu_N/ZSM-5 catalysts; (*F*) Reaction order of NH_3 for the Cu_S/ZSM-5 and Cu_N/ZSM-5 catalysts.

and Cu_M/ZSM-5 (*SI Appendix*, Fig. S5). The Cu loading in Cu_S/ZSM-5 and Cu_N/ZSM-5 was quantified using microwave plasma atomic emission spectrometry (MP-AES) (*SI Appendix*, Table S2).

Catalytic Studies. With the same Cu loading of 4 wt%, Cu_S/ZSM-5 has the highest activity and selectivity to N_2 in the NH_3–SCO reaction among the three catalysts (Fig. 2 *A* and *B* and *SI Appendix*, Fig. S6). The catalyst performance of Cu_N/ZSM-5 is generally inferior to that of Cu_S/ZSM-5 across all temperatures,

and Cu_M/ZSM-5 displays intermediate activity. NH_3 conversion employing Cu_S/ZSM-5 reaches a value of 93% with high selectivity to N_2 (92%) at 350 °C, compared to Cu_N/ZSM-5 which has a lower activity and selectivity to N_2 of 85 and 73%, respectively. Stabilization of SSs was validated from continuous on-stream testing for 100 h at 300 °C (Fig. 2*C*). The apparent activation energy (E_a) of Cu_S/ZSM-5 is 58 kJ/mol (Fig. 2*D*), which is much lower than Cu_N/ZSM-5 (126.8 kJ/mol). Additionally, the reaction orders for O_2 and NH_3 differ for Cu_S/ZSM-5 and Cu_N/ZSM-5. The higher reaction order of O_2 with Cu_S/ZSM-5 suggests that

Fig. 3. Evaluation of Cu_S/ZSM-5 with different Cu loadings as catalysts in NH_3–SCO. (*A* and *B*) NH_3 conversion and N_2 selectivity as a function of temperature (reaction conditions: 50 mg catalyst, 2,000 ppm NH_3, 5% O_2 balanced in He, gas flow 100 mL/min, WHSV 240 mL NH_3 h^{-1} g^{-1}); (*C*) NH_3 conversion as a function of the Cu loading; (*D*) EPR spectra of Cu_S/ZSM-5 with different Cu loadings; (*E*) Proportion of Cu SSs in Cu_S/ZSM-5 at different Cu loadings; (*F*) TOF for Cu_S/ZSM-5 with different Cu loadings (Cyan dots: TOF for CuO NPs in $Cu_{10\%}$/ZSM-5. The X-axis corresponds to the amount of CuO NPs in mmol).
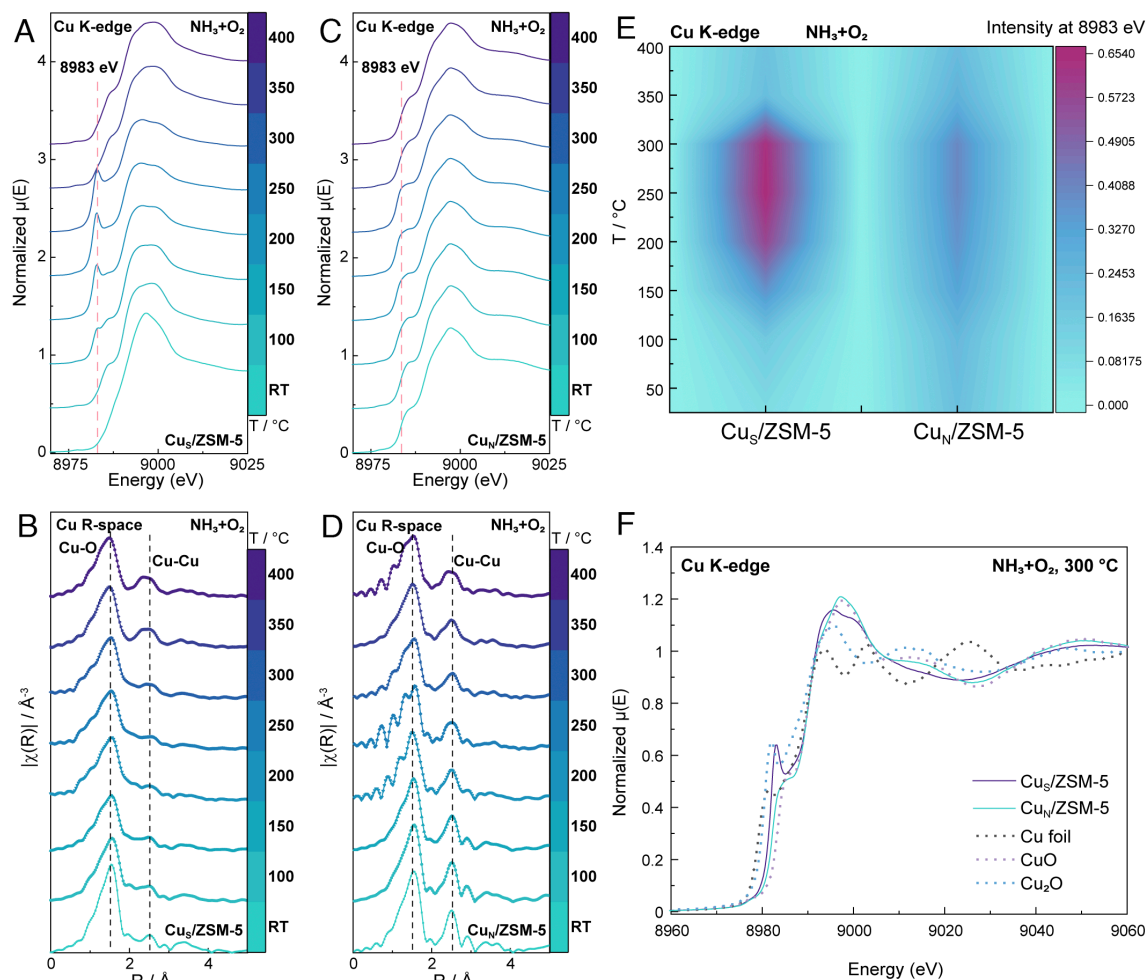
**Fig. 4.** Operando Cu K-edge XAFS spectra of Cu_S/ZSM-5 and Cu_N/ZSM-5. (*A* and *B*) Operando Cu K-edge XANES spectra of Cu_S/ZSM-5 and Cu_N/ZSM-5 as a function of temperature [dashed line at 8,983 eV is the typical feature of $Cu^I(NH_3)_2$]; (*C* and *D*) Operando R space spectra of Cu_S/ZSM-5 and Cu_N/ZSM-5 as a function of temperature (dashed lines at 1.5 and 2.5 Å corresponding to Cu–N/O and Cu–Cu scattering in CuO, respectively); (*E*) Signal intensity of the Cu^I s-4p transition peak at 8,983 eV. (*F*) Operando Cu K-edge XANES spectra of Cu_S/ZSM-5 and Cu_N/ZSM-5 at 300 °C. All spectra were recorded in 5,000 ppm NH_3, 5% O_2, balanced in He.

higher O_2 concentration favors the reaction rate (Fig. 2*E*). The negative reaction order of NH_3 with Cu_S/ZSM-5 indicates that NH_3 coordinates to the Cu(II) sites, inhibiting O_2 binding (Fig. 2*F*). The activity and selectivity of Cu_S/ZSM-5 increases with the Cu loading (Fig. 3 *A* and *B* and *SI Appendix*, Fig. S7). Cu SSs are the predominant active Cu species at loadings <4 wt% (Fig. 3 *D* and *E*). At 225 and 250 °C the catalytic performance improves almost proportionally as the Cu loading increases to 4 wt% (Fig. 3*C*), with the turnover frequency (TOF) remaining constant at Cu loadings below 4 wt% (Fig. 3*F*). Such catalytic behavior suggests atomically dispersed Cu sites are the main active species. At a Cu loading of 10 wt% ($Cu_{10\%}$/ZSM-5), only 23% of the Cu species comprise Cu SSs (Fig. 3*E*), leading to a nonproportional increase in activity (Fig. 3*C*). Indeed, the TOF of the CuO NPs in $Cu_{10\%}$/ZSM-5 is lower than the average TOF of the Cu SSs (Fig. 3*F*), confirming that CuO NPs are less active than Cu SSs.

Redox Behavior of Cu SSs and CuO NPs. The geometric and electronic structures of the active Cu species were investigated under actual reaction conditions using operando Cu K-edge XAFS spectroscopy (Fig. 4 and *SI Appendix*, Fig. S8). Between 200 and 300 °C, Cu_S/ZSM-5 is partially reduced to Cu^I under NH_3 + O_2, verified by a peak at Cu K-edge 8,983 eV [the typical feature for $Cu^I(NH_3)_2$ 1 s → 4p XANES], which is considerably more intense in Cu_S/ZSM-5

compared to Cu_N/ZSM-5 (Fig. 4 *A*, *E*, and *F*). In the light off curve of Cu_S/ZSM-5 shown in *SI Appendix*, Fig. S9, the reaction rate increases rapidly from 200 °C, which corresponds to the formation temperature of the $Cu^I(NH_3)_2$ species (Fig. 4*E*). $Cu^I(NH_3)_2$ species might be the main active intermediate in NH_3–SCO, which follows the internal SCR mechanism in which $Cu^I(NH_3)_2$ is also the key active species. Above 300 °C, the $Cu^I(NH_3)_2$ feature at 8,983 eV in Cu_S/ZSM-5 disappears along with an increase in the white-line intensity at 8,996 eV (Fig. 4 *A* and *E*), indicating oxidation to Cu^{II}. The weak adsorption band at 1,565 cm^{-1} may be assigned to $Cu^I(NH_3)_2$ in the operando DRIFTS data (*SI Appendix*, Fig. S10) (24). When the temperature is <250 °C, the $Cu^I(NH_3)_2$ species is observed, which is known to be an important intermediate for the NH_3-SCR reaction at low temperatures (24). When the temperature is <250 °C, the $Cu^I(NH_3)_2$ species is observed, which is known to be an important intermediate for the NH_3-SCR reaction at lower temperatures (24). $[Cu^I(NH_3)_2]^+$ species are weakly bound to the zeolite (25), and the mobility of $[Cu^I(NH_3)_2]^+$ facilitates the formation of the dimeric species $[Cu_2(NH_3)_4O_2]^{2+}$, thus enabling the activation and dissociation of O_2 (26, 27) $[Cu_2(NH_3)_4O_2]^{2+}$ reacts with NH_3 to form zjr superoxo $[Cu^{II}(NH_3)_3(OO^*)]^+$ complex and $[Cu^I(NH_3)_2]^+$, i.e., $[Cu_2(NH_3)_4O_2]^{2+}$ + NH_3 → $[Cu^{II}(NH_3)_3(OO^*)]^+$ + $[Cu^I(NH_3)_2]^+$ (28). Complete restoration of $[Cu^I(NH_3)_2]^+$ confirms the reversibility of the oxidation of the $[Cu^I(NH_3)_2]^+$ species, underlining it as a highly redox active species.
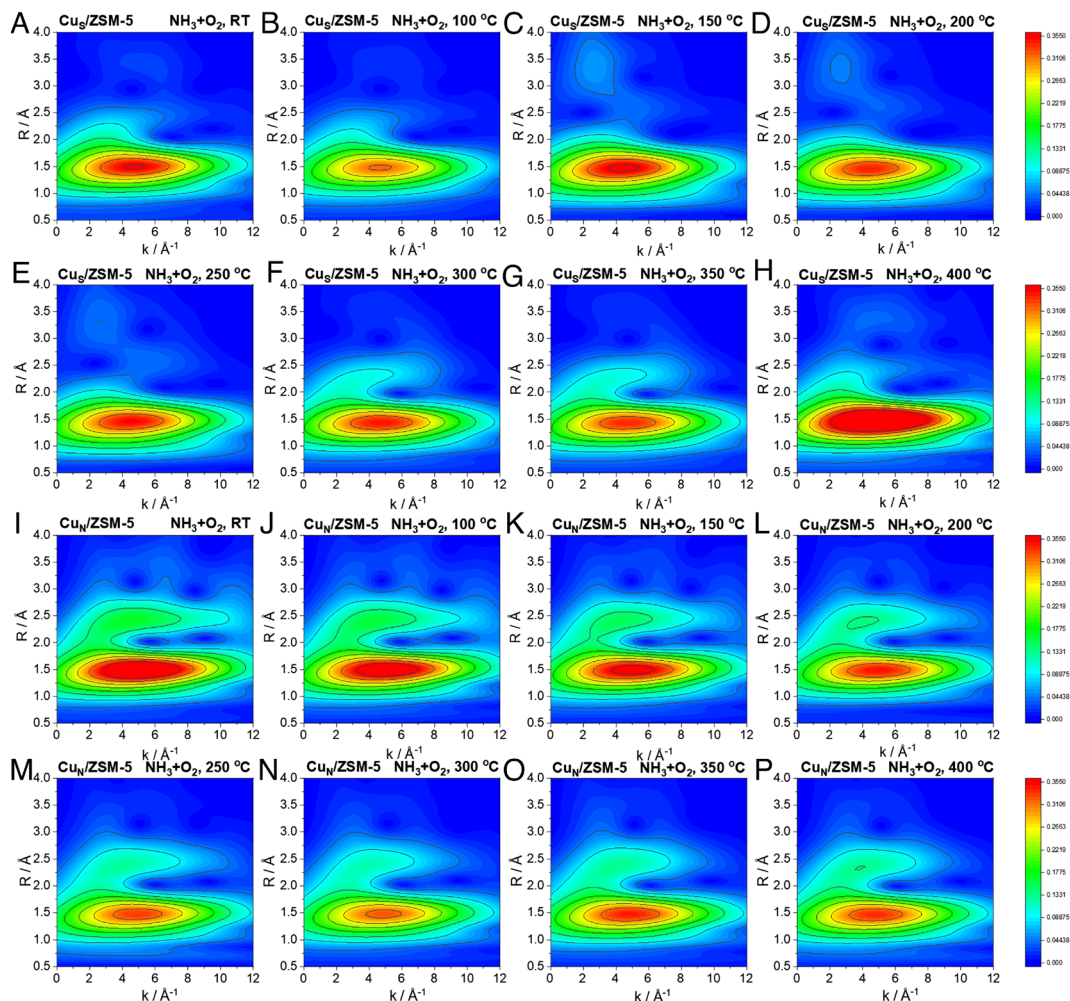
Fig. 5. Operando 2D WT-EXAFS maps of Cu$_S$/ZSM-5 and Cu$_N$/ZSM-5 in NH$_3$ and O$_2$ at different temperatures. Cu$_S$/ZSM-5 at RT (*A*), 100 °C (*B*), 150 °C (*C*), 200 °C (*D*), 250 °C (*E*), 300 °C (*F*), 350 °C (*G*), and 400 °C (*H*); Cu$_N$/ZSM-5 at RT (*I*), 100 °C (*J*), 150 °C (*K*), 200 °C (*L*), 250 °C (*M*), 300 °C (*N*), 350 °C (*O*), and 400 °C (*P*). All spectra measured in 5,000 ppm NH$_3$, 5% O$_2$ balanced in He.

In comparison, the oxidation state of Cu in the NPs in Cu$_N$/ZSM-5 hardly changes over the entire temperature range. Compared with Cu$_N$/ZSM-5, the ability to form Cu^I(NH$_3$)$_2$ under SCO conditions explains the superior catalytic performance of Cu$_S$/ZSM-5.

The aggregation of SSs to NPs and the redispersion of NPs to SSs during reaction have been widely discussed (29–31). Thus, it is important to identify the Cu species present under different reaction conditions. The differences in the aggregation state of Cu were determined during reaction by the Fourier-transformed EXAFS, which contains features at 1.5 and 2.5 Å corresponding to Cu–N/O and Cu–Cu scattering, respectively. The absence of a Cu–Cu scattering feature in Cu$_S$/ZSM-5 confirms the thermal stability of the Cu SSs over the entire temperature range (Fig. 4*C*). In comparison, a peak at 2.5 Å corresponding to Cu–O–Cu was observed in Cu$_N$/ZSM-5, which indicates that CuO NPs are the dominant species and are stable (Fig. 4*D*). Furthermore, Cu$_S$/ZSM-5 has a smaller Cu–Cu coordination number (C.N.) of 0.79 ± 0.46, compared to Cu$_N$/ZSM-5. There are two types of Cu–Cu scatterings in Cu$_N$/ZSM-5, Cu–Cu (1) with a C.N. of 3.57 ± 0.55 and Cu–Cu (2) with a C.N. of 2.19 ± 0.41 (*SI Appendix*, Fig. S11 and Table S1). A smaller overall coordination number indicates that most Cu sites in the Cu$_S$/ZSM-5 are SSs, whereas most Cu sites are in the form of NPs in Cu$_N$/ZSM-5. After reaction, the Cu–Cu C.N. of Cu$_S$/ZSM-5 is similar to that before reaction (*SI Appendix*, Fig. S12 and Table S1), which demonstrates the thermal stability

of the Cu SSs in Cu$_S$/ZSM-5. Overall, the operando Cu K-edge EXAFS shows that Cu SSs are the predominant active sites in Cu$_S$/ZSM-5. With different active sites and different active species, the two catalysts display different activities in the NH$_3$–SCO reaction.

In parallel, WT analysis (32) of the EXAFS spectra leads to a 2D representation of the EXAFS, simultaneously revealing the signal features in both R- and k-space. As shown in Fig. 5, Cu$_S$/ZSM-5 contains a distinct first shell peak (centered at 4.5 Å^{-1}, 1.5 Å), which is associated with contributions from framework (fw) oxygen atoms. For the second shell sphere [R(Å) > 2 Å], the higher lobe at (6.0 Å^{-1}, 3.3 Å) is well-resolved due to the different backscattering properties of various atoms, which strongly depend on the atomic number. This lobe may be attributed to the signals from the Si and/or Al atoms of the framework. As the temperature is increased to 150 °C, a decrease of signals from the Si/Al atoms of the framework suggests the formation of Cu^I(NH$_3$)$_2$ (28, 33, 34), in agreement with the XANES and EXAFS results (Fig. 4). A moderately intense sublobe is observed in the low-k range, characteristic of low-Z (O or N) scatterers. The pivotal stage in activating oxygen involves the isothermal oxidation of the [Cu^I(NH$_3$)$_2$]$^+$ species (28), as depicted in the WT analysis presented in Fig. 5 *E* and *F*. The higher-k lobe at 7.0 Å^{-1} probably results from the scattering of the second shell Cu species, since oxygen-bridged Cu dimers are formed after Cu^I(NH$_3$)$_2$ oxidation by O$_2$ (35). At higher temperatures (300 to 350 °C), a higher signal for the lobe at ~7.0 Å^{-1}

indicates that more Cu^I species are oxidized into Cu^{II} ions. At 400 °C, the signal for Cu–Cu scattering decreases, whereas the Cu–Si/Al scattering [i.e., Si and Al from the ZSM-5 framework (fw)] signal increases, suggesting the formation of the framework of fw-Cu^{II} zeolite (26, 27). In comparison, Cu$_N$/ZSM-5 has a pronounced Cu–Cu scattering lobe (centered at 5 Å^{-1}, 2.2 Å) at all temperatures, in addition to Cu–O scattering (centered at 4.5 Å^{-1}, 1.3 Å). The Cu–Cu scattering lobe further confirms the presence and the stability of CuO NPs in Cu$_N$/ZSM-5.

The Cu K-edge XAFS spectra were further compared by altering the gas phase during operando measurements, i.e., from NH$_3$ + O$_2$ to NH$_3$ to NH$_3$ + O$_2$ and finally O$_2$ (*SI Appendix*, Fig. S13). In NH$_3$, the peak at Cu K-edge 8,983 eV [Cu^I(NH$_3$)$_2$] is considerably more intense in Cu$_S$/ZSM-5, compared with that in Cu$_N$/ZSM-5 (*SI Appendix*, Fig. S13). Switching to NH$_3$ + O$_2$ and O$_2$ gas feeds led to different degrees of Cu(I) oxidation, suggesting a redox mechanism for the SCO reaction. WT analysis further validated the presence of Cu^I(NH$_3$)$_2$ in Cu$_S$/ZSM-5 (*SI Appendix*, Fig. S14).

Conclusions

We successfully synthesized thermally stable single Cu sites-based catalysts, Cu$_S$/ZSM-5, with high loadings, using a facile two-step method. The Cu$_S$/ZSM-5 catalyst shows excellent activity and selectivity to N$_2$ in the NH$_3$–SCO reaction. Through a comparative analysis of the performance between Cu SSs and CuO NPs in NH$_3$–SCO, a clear size dependency is observed, with monodisperse Cu atoms being advantageous. The difference in the activation energy and reaction order between Cu SSs and CuO NPs strongly implies that they operate via different reaction mechanisms. Operando XAFS studies combined with WT analysis reveal structure–performance relationships, elucidating subtle changes in the active sites under actual working conditions. Specifically, Cu SSs facilitate the formation of Cu^I(NH$_3$)$_2$ species, identified as a key active intermediate, and exhibit enhanced redox processes that facilitate the NH$_3$–SCO redox reaction.

Materials and Methods

Materials. Cu(NO$_3$)$_2$·3H$_2$O and NaBH$_4$ were purchased from Sigma Aldrich, and ZSM-5 was purchased from Zeolyst. All chemicals are used as received.

Catalyst Preparation.

Synthesis of CuS/ZSM-5. ZSM-5 (0.5 g, Si/Al = 11.5) was dispersed in ethanol (20 mL) under vigorous stirring at room temperature. To the resulting suspension, a solution containing Cu(NO$_3$)$_2$·3H$_2$O (79.2 mg for 4 wt% Cu loading, and it changes with different Cu loading) in ethanol (5 mL) was slowly added, and stirring was continued for 12 h at room temperature. The reaction mixture was then heated at 40 °C under stirring until all the solvent had evaporated. The remaining solid was heated to 300 °C for 1 h under 15% H$_2$/Ar at 5 °C/min in a tube furnace. The solid was then heated to 500 °C for 5 h at 5 °C/min in air in a Muffle furnace to afford Cu$_S$/ZSM-5.

Synthesis of CuN/ZSM-5. Solution A, Cu(NO$_3$)$_2$·3H$_2$O (79.2 mg) in degassed H$_2$O (5 mL), was stirred under N$_2$ at 0 °C for 10 min. Solution B, NaBH$_4$ (6 mg) in degassed H$_2$O (5 mL), was added to the Solution A. After stirring for 1 h at 0 °C, ZSM-5 (0.5 g) was added while stirring for 1 h. Next, the solid was washed with ethanol (5 × 30 mL) and collected by centrifugation. After drying at 60 °C for 24 h, the solid was heated to 500 °C for 5 h at 5 °C/min in air in a Muffle furnace to afford Cu$_N$/ZSM-5.

Synthesis of CuM/ZSM-5. Cu(NO$_3$)$_2$·3H$_2$O (79.2 mg) and ZSM-5 (0.5 g) were ground for 15 min, and the resulted mixture was heated to 500 °C for 5 h at 5 °C/min in air in a Muffle furnace to afford Cu$_M$/ZSM-5.

Ex Situ Characterization. EPR spectroscopy: Experiments were performed in continuous-wave (cw) mode on a Bruker E580 X-band EPR spectrometer equipped with a Bruker ER4122-SHQE cavity. Then, 20 mg powder of each sample

was loaded into a high-purity quartz EPR tube (4.0 mm o.d., 3.0 mm i.d.) for measurements. All cw EPR spectra were acquired at room temperature over a wide magnetic field range. Typical spectrometer parameters were sweep time (300 s), center field (300 mT), sweep width (300 mT), modulation frequency (100 kHz), microwave frequency (9.87 GHz), and microwave power (2.0 mW).

XRD: XRD patterns were recorded on a StadiP diffractometer (STOE) with a Mo (Kα = 0.7093165 Å) radiation. The operating voltage and current were 40 kV and 30 mA, respectively. 2θ in the range of 2 to 40° were collected with a resolution of 0.015° for each step.

X-ray photoelectron (XPS) spectroscopy was performed on Thermoscientific instrument using an Al Kα source (1,486.6 eV). All peaks were calibrated using adventitious C 1 s peak of 284.8 eV to correct charge shift of binding energies after deconvolution.

MP-AES: The Cu loading in the catalysts was determined using an Agilent 4100 MP-AES (USA). Commercial Cu(NO$_3$)$_2$ standard solutions were used for the calibration. The catalysts were dissolved in HNO$_3$ solution and were diluted to around 1,000 ppm and filtered before analysis.

STEM: Aberration-corrected BF and annular dark field (ADF) STEM was performed on a JEOL ARM300CF (E02) (Tokyo, Japan) transmission electron microscope operating 300 kV. Simultaneous energy dispersive X-ray (EDX) spectroscopy and aberration-corrected BF/ADF-STEM imaging was performed on a JEOL ARM200CF (E01) operating at 200 kV and equipped with JEOL dual silicon drift detectors at the electron Physical Sciences Imaging Centre (ePSIC) at the Diamond Light Source (UK) (DLS). The ARM300CF operated with a convergence semiangle of 26.2 mrad and BF and ADF collection semiangles of 0 to 31.6 and 77.0 to 209.4 mrad, respectively. The ARM200CF operated with a convergence semiangle of 23.0 mrad with BF and ADF collection semiangles of 0 to 21.9 and 37.5 to 128.3 mrad, respectively. Single-pass EDX spectra were collected with drift correction. Data were acquired and processed using the Gatan Microscopy Suite (a.k.a. Digital Micrograph) (36). Nanoscale catalyst particles were prepared via a standard preparation route: A small amount (<5 mg) of catalyst powder was dispersed in approximately 1 mL ethanol, after sonication and drop casting onto holey carbon-coated gold TEM support grids. Gold was used instead of the more typical copper grid to avoid overlapping fluorescent signals with the sample during EDX mapping. The average particle size was calculated based on more than 50 particles for each sample.

Operando Cu K-Edge XAFS. XAFS of Cu K-edge (8.979 keV) was carried out on the BL14B2 beamline at Spring8 (Japan). Spectra were recorded in transmission mode with a Si(111) double-crystal monochromator. In the operando experiments, 100 mg catalyst was pressed into a pellet (diameter 10 mm) and measurements were conducted in an in situ cell at BL14B2 (Hard X-ray bending magnet beamline in Spring-8, Japan). For operando XAFS at different temperatures, the pellet was exposed to 5,000 ppm NH$_3$ and 5% O$_2$ balanced in He and heated from 30 to 450 °C. For operando XAFS in different gases, the pellet was exposed to NH$_3$ (5,000 ppm NH$_3$ balanced in He), then exposed in NH$_3$+O$_2$ (5,000 ppm NH$_3$, 5% O$_2$ balanced in He), and finally exposed to O$_2$ (5% O$_2$ balanced in He), and the temperature was maintained at 300 °C. The total gas flow rate was 120 mL min^{-1}. Spectra were recorded after stabilizing for at least 10 min after attaining a steady state at each reaction temperature. Cu foil standards were used for energy shift calibration. Three spectra were merged to improve signal quality. XAFS data were performed using the Demeter software package (including Athena and Artemis) (37). Athena software was used for XANES analysis. Artemis software was used to fit the k^2-weighted EXAFS data in real space with 3.0 Å^{-1} < k < 12.0 Å^{-1} and 1.0 Å < R < 3.3 Å. The calculated amplitude reduction factor S$_0^2$ from EXAFS analysis of Cu foil was 0.878, which was used as a fixed parameter for EXAFS fitting. The coordination number and bond length were calculated based on the reported structure from Crystal open database: Cu (No.9013014), CuO (No. 1011148).

Operando DRIFTS. DRIFTS were performed using a PerkinElmer Frontier FT-IR Spectrometer. The sample was heated in He at 350 °C for 30 min to remove surface contamination. After cooling to room temperature, the sample was exposed to 5,000 ppm NH$_3$ and 5%O$_2$/He for 10 min, during which spectra were recorded. Then, the sample was heated up from 30 to 450 °C with a ramp of 10 °C/min. The spectra were recorded from 4,400 to 500 cm^{-1} with a resolution of 2 cm^{-1}. Background DRIFTS spectra were recorded in He and subtracted from the sample spectrum for each measurement.

Catalytic Tests. The performance of the catalysts in NH_3–SCO was evaluated in a fixed-bed flow reactor at a gas flow rate of 100 mL/min, consisting of 5,000 ppm NH_3, 5 vol% O_2, and a He balance. Typically, 50 mg catalyst was placed in the reaction tube, and quantification of products was performed with an online Quadrupole Mass Spectrometer Quantitative Gas Analyser (Hiden Analytical, UK). The reaction was investigated at temperatures ranging from 150 to 450 °C. The reaction was kept stable for 30 min after attaining a steady state at each reaction temperature to detect the signals derived from the substrates (NH_3 and O_2) and products (N_2, N_2O, and NO). After cooling to room temperature, the postcatalysts were denoted as Cu_5/ZSM-5 AR (after reaction) and used for postcatalysis characterization.

To estimate the activation energy, 50 mg catalyst powder was placed in a fixed-bed flow reactor operating at a gas flow rate of 100 mL/min, consisting of 5,000 ppm NH_3, 5 vol% O_2, and a He balance. The reaction was investigated at temperatures ranging from 200 to 260 °C.

To obtain the reaction order of NH_3, the O_2 concentration was kept as 5%, and the concentration of NH_3 was varied. i.e., 2,500, 4,500, 6,000, 7,500, and 9,000 ppm. All tests were performed at 220 °C.

The reaction order of O_2 was obtained by keeping the NH_3 concentration constant at 5,000 ppm, and the concentration of O_2 was varied from 5 to 9%. All the tests were performed at 220 °C.

Author affiliations: [a]Department of Chemical Engineering, University College London, London WC1E 7JE, United Kingdom; [b]Institute of Chemical Sciences and Engineering, École Polytechnique Fedérale de Lausanne (EPFL), Lausanne CH-1015, Switzerland; [c]Department of Applied Chemistry, Faculty of Science and Engineering, Kindai University, Higashi-Osaka, Osaka 577-8502, Japan; [d]electron Physical Science Imaging Center, Diamond Light Source Ltd., Didcot OX11 0DE, United Kingdom; [e]Department of Materials, University of Oxford, Oxford OX1 3PH, United Kingdom; and [f]United Kingdom Catalysis Hub, Research Complex at Harwell, Rutherford Appleton Laboratory, Harwell OX11 0FA, United Kingdom

Author contributions: L.C., X.G., P.J.D., and F.R.W. designed research; L.C., X.G., performed research; L.C., X.W., H.A., C.A., D.G.H., and J.C. contributed analytic tools; L.C. and X.G. analyzed data; and L.C. and P.J.D. wrote the paper.

1. A. Wang, J. Li, T. Zhang, Heterogeneous single-atom catalysis. *Nat. Rev. Chem.* **26**, 65–81 (2018).
2. S. K. Kaiser, Z. Chen, D. Faust Akl, S. Mitchell, J. Pérez-Ramírez, Single-atom catalysts across the periodic table. *Chem. Rev.* **120**, 11703–11809 (2020).
3. R. Lang *et al.*, Single-atom catalysts based on the metal-oxide interaction. *Chem. Rev.* **120**, 11986–12043 (2020).
4. L. Liu, A. Corma, Metal catalysts for heterogeneous catalysis: From single atoms to nanoclusters and nanoparticles. *Chem. Rev.* **118**, 4981–5079 (2018).
5. H. Huang, K. Shen, F. Chen, Y. Li, Metal-organic frameworks as a good platform for the fabrication of single-atom catalysts. *ACS Catal.* **10**, 6579–6586 (2020).
6. J. Guo *et al.*, A minireview on the synthesis of single atom catalysts. *RSC Adv.* **12**, 9373–9394 (2022).
7. S. Ma, W. Han, W. Han, F. Dong, Z. Tang, Recent advances and future perspectives in MOF-derived single-atom catalysts and their application: A review. *J. Mater. Chem. A* **11**, 3315–3363 (2023).
8. C. Mondelli *et al.*, Biomass valorisation over metal-based solid catalysts from nanoparticles to single atoms. *Chem. Soc. Rev.* **49**, 3764–3782 (2020).
9. Z. Li *et al.*, Well-defined materials for heterogeneous catalysis: From nanoparticles to isolated single-atom sites. *Chem. Rev.* **120**, 623–682 (2020).
10. P. Serna *et al.*, Single-site vs. cluster catalysis in high temperature oxidations. *Angew. Chem. Int. Ed. Engl.* **133**, 16090–16098 (2021).
11. E. K. Dann *et al.*, Structural selectivity of supported Pd nanoparticles for catalytic NH3 oxidation resolved using combined operando spectroscopy. *Nat. Catal.* **2**, 157–163 (2019).
12. D. Decarolis *et al.*, Spatial profiling of a Pd/Al2O3 catalyst during selective ammonia oxidation. *ACS Catal.* **11**, 2141–2149 (2021).
13. H. Wang *et al.*, Selective catalytic oxidation of ammonia over nano Cu/zeolites with different topologies. *Environ. Sci. Nano* **7**, 1399–1414 (2020).
14. M. Jabłońska, Progress on selective catalytic ammonia oxidation (NH 3 -SCO) over Cu−containing zeolite-based catalysts. *ChemCatChem* **12**, 4490–4500 (2020).
15. F. Han *et al.*, Formation of highly active superoxide sites on CuO nanoclusters encapsulated in SAPO-34 for catalytic selective ammonia oxidation. *ACS Catal.* **9**, 10398–10408 (2019).
16. T. Zhang, H. Chang, Y. You, C. Shi, J. Li, Excellent activity and selectivity of one-pot synthesized Cu-SSZ-13 catalyst in the selective catalytic oxidation of ammonia to nitrogen. *Environ. Sci. Technol.* **52**, 4802–4808 (2018).
17. X. Cui *et al.*, Selective catalytic oxidation of ammonia to nitrogen over mesoporous CuO/RuO2 synthesized by co-nanocasting-replication method. *J. Catal.* **270**, 310–317 (2010).
18. Z. Wang *et al.*, Selective catalytic oxidation of ammonia to nitrogen over CuO-CeO2 mixed oxides prepared by surfactant-templated method. *Appl. Catal. B Environ.* **134–135**, 153–166 (2013).
19. H. Sjövall, R. J. Blint, L. Olsson, Detailed kinetic modeling of NH3 SCR over Cu-ZSM-5. *Appl. Catal. B Environ.* **92**, 138–153 (2009).
20. X. Guo *et al.*, Outstanding low-temperature performance for NH3-SCR of NO over broad Cu-ZSM-5 sheet with highly exposed a-c orientation. *Appl. Catal. B Environ.* **343**, 123519 (2024).
21. M. Rutkowska *et al.*, Catalytic performance of commercial Cu-ZSM-5 zeolite modified by desilication in NH 3 -SCR and NH 3 -SCO processes. *Microporous Mesoporous Mater.* **246**, 193–206 (2017).
22. C. Zhong *et al.*, Design, synthesis, and insights into the redox mechanism of highly efficient one-pot Cu-ZSM-5 catalysts for the reduction of NO x by NH 3 -SCR at low temperatures. *ACS Catal.* **13**, 10927–10944 (2023).
23. X. Guan *et al.*, Designing reactive bridging O2-at the atomic Cu-O-Fe site for selective NH3 oxidation. *ACS Catal.* **12**, 15207–15217 (2022).
24. H. Wang *et al.*, Highly efficient NO abatement over Cu-ZSM-5 with special nanosheet features. *Environ. Sci. Technol.* **55**, 5422–5434 (2021).
25. K. A. Lomachenko *et al.*, The Cu-CHA deNOx catalyst in action: Temperature-dependent NH3-assisted selective catalytic reduction monitored by operando XAS and XES. *J. Am. Chem. Soc.* **138**, 12025–12028 (2016).
26. L. Chen, H. Falsig, T. V. W. Janssens, H. Grönbeck, Activation of oxygen on (NH3–Cu–NH3)+ in NH3-SCR over Cu-CHA. *J. Catal.* **358**, 179–186 (2018).
27. F. Gao, D. Mei, Y. Wang, J. Szanyi, C. H. F. Peden, Selective catalytic reduction over Cu/SSZ-13: Linking homo- and heterogeneous catalysis. *J. Am. Chem. Soc.* **139**, 4935–4942 (2017).
28. C. Negri *et al.*, Structure and reactivity of oxygen-bridged diamino dicopper(II) complexes in Cu-ion-exchanged chabazite catalyst for NH 3 -mediated selective catalytic reduction. *J. Am. Chem. Soc.* **142**, 15884–15896 (2020).
29. X. Wei *et al.*, Dynamic reconstitution between copper single atoms and clusters for electrocatalytic urea synthesis. *Adv. Mater.* **35**, 1–8 (2023).
30. M. Moliner *et al.*, Reversible transformation of Pt nanoparticles into single atoms inside high-silica chabazite zeolite. *J. Am. Chem. Soc.* **138**, 15743–15750 (2016).
31. S. Feng *et al.*, In situ formation of mononuclear complexes by reaction-induced atomic dispersion of supported noble metal nanoparticles. *Nat. Commun.* **10**, 1–9 (2019).
32. J. Timoshenko, A. Kuzmin, Wavelet data analysis of EXAFS spectra. *Comput. Phys. Commun.* **180**, 920–925 (2009).
33. Y. Shan *et al.*, Strikingly distinctive NH3-SCR behavior over Cu-SSZ-13 in the presence of NO2. *Nat. Commun.* **131**, 1–10 (2022).
34. A. Martini *et al.*, Assessing the influence of zeolite composition on oxygen-bridged diamino dicopper(II) complexes in Cu-CHA DeNOx catalysts by machine learning-assisted X-ray absorption spectroscopy. *J. Phys. Chem. Lett.* **13**, 6164–6170 (2022).
35. C. Paolucci *et al.*, Dynamic multinuclear sites formed by mobilized copper ions in NO x selective catalytic reduction. *Science* **357**, 898–903 (2017).
36. Gatan, Inc., United States of America, DigitalMicrograph Software. https://www.gatan.com/products/tem-analysis/gatan-microscopy-suite-software. Accessed 1 May 2024.
37. B. Ravel, M. Newville, ATHENA, ARTEMIS, HEPHAESTUS: Data analysis for X-ray absorption spectroscopy using IFEFFIT. *J. Synchrotron Radiat.* 12, 537–541 (2005).